



A diffusive dynamic brittle fracture model for heterogeneous solids and porous materials with implementation using a user-element subroutine

Udit Pillai^{b,1}, Yousef Heider^{a,*}, Bernd Markert^a

^a Institute of General Mechanics, RWTH Aachen University, Templergraben 64, 52062 Aachen, Germany

^b Centre for Structural Engineering and Informatics, Faculty of Engineering, University of Nottingham, Nottingham NG7 2RD, UK

ARTICLE INFO

Keywords:

Hydraulic fracturing
Phase-field modelling
Porous media
ABAQUS user subroutines
Weibull distribution

ABSTRACT

This paper addresses brittle fracture simulation using the phase-field modelling (PFM) as an effective and prominent method to predict crack onset and topology in heterogeneous solids and porous materials. This includes the study of the significant crack behaviour change due to the inhomogeneous nature of the materials, where the Weibull distribution is used for creating spatial variations of the material properties. The permanent changes in the permeability and volume fractions of the individual constituents in the cracked porous domain are appropriately accounted for. The present work combines the well-established macroscopic Theory of Porous Media (TPM) and the PFM by means of a user element (UEL) in the software ABAQUS. The coupled system of TPM and PFM equations is then solved in a monolithic fashion for both homogeneous and heterogeneous cases. Numerical examples present a comparative study demonstrating the difference in fracture patterns between homogeneous and heterogeneous solids and porous cases.

1. Introduction

Prediction of failure mechanisms involving crack initiation and propagation is of prime importance in many engineering fields, which are related to production and safety assessment. One of the prominent applications is hydraulic fracturing, applied in enhanced geothermal systems (EGS) through injection of high-pressure water into deep rock layers in order to enhance the rock's low permeability. Another important application, is hydraulic fracturing process (fracking) prevalent in oil and gas industries to extract unconventional natural resources, like shale gas, petroleum and brine from deep rock formations. Hydraulic fracturing also has applications in geomechanics to study the stability of dams. In the underlying research work, the phase-field modelling (PFM) is employed for fracture modelling, which is an energy-based diffusive crack approach scheme with an internal length-scale parameter that controls the amount of diffusion. The PFM uses a scalar phase-field variable, which indicates the cracked state of a material. Moreover, the PFM has proved its relevance in predicting brittle fractures by simulating complex crack patterns including crack initiation, branching and merging. Several studies have been conducted in the past to establish a complete theoretical and numerical framework and to gain more understanding and control of fracturing processes in pure solids and in porous materials.

In the early developments for depicting brittle solid fractures, Griffith [28] treated crack propagation with an elastic energy-based approach and related it to a critical energy release rate, which marked the foundation of the classical theory of brittle fracture. Irwin [32] further extended the classical theory by proposing a new criterion for crack initiation and established a relationship between factors, like the strain energy release rate or the fracture work rate, and the elastic stresses and strains near the leading edge of brittle cracks. In earlier works based on discrete crack models, a crack was incorporated as a geometrical entity and the crack path was constrained only to the element edges. For complex crack patterns and coarser meshes, this lead to a significant overestimation of the fracture energy when the true crack path deviated from the predicted crack path (Msekh et al. [51]). An important milestone in the crack initiation and propagation modelling was achieved with the development of the extended finite element methods (XFEM) by Belytschko and Black [6], Moës and Belytschko [50]. XFEM, based on the generalised finite element method, enables a local enrichment of the approximation space via the partition of unity method, which equips it with huge flexibility in predicting the true stress behaviour and resolving stress singularities at the crack tip. However, XFEM requires a pair of level set functions to be defined for each individual crack segment and faces serious computational challenges in cases of complex models with additional degrees of freedom

* Corresponding author.

E-mail address: heider@iam.rwth-aachen.de (Y. Heider).

¹ These authors contributed equally to this work.

and for the case of closing cracks, where contact formulations have to be included.

Phase-field modelling of fracture, which relies on a variational model of crack evolution, was first proposed in the work of Francfort and Marigo [27] in the late 1990s to get rid of the constraints posed by classical Griffith's theory, like pre-existing and well-defined crack paths. This approach was later implemented numerically by Bourdin et al. [12]. Important contributions were made by Miehe et al. [42], Kuhn and Müller [33] within the variational framework by simulating multi-dimensional fractures involving mixed-modes with dynamic effects. In Aldakheel et al. [4], an important extension towards ductile fracture using Gurson-type plasticity at finite strain can be found. Additional applications and PFM-related solution schemes can be also found in, e.g., Ambati et al. [5], Patil et al. [52], Ehlers and Luo [25], Weinberg and Hesch [59], Cajuhi et al. [16], Miehe et al. [44,41] among others. Msekhi et al. [51] implemented the PFM for homogeneous brittle solid fractures combining UEL and UMAT subroutines in the commercial FEM software ABAQUS and highlighted the implementation details. Later, Liu et al. [36] solved the coupled PFM problem using ABAQUS by monolithic and sequentially staggered schemes and compared the two methods on scales of accuracy, computational efficiency and sensitivity to mesh sizes.

With reference to porous media, different fundamental theories describing the constitutive behaviour of multiphase continua have been given in literature. The most prominent amongst those are the approach developed by Biot [7–9] and the Theory of Porous Media (TPM) established by Bowen [13,14], De Boer [20] and Ehlers [22–24]. The TPM considers a macroscopic continuum approach based on the mixture theory, see Truesdell [58] and Bowen [13,14], wherein the overall continuum consists of spatially superimposed solid and liquid phases coupled with each other through interaction terms. Simulation of hydraulic fracturing in porous media poses multiple modelling challenges, including treatment of the solid and liquid phases and their interaction during pre- and post-crack regimes, incorporating changes of permeability and volume fractions during crack propagation. Additionally, the fluid flow needs to be modelled appropriately, accounting for its change from Darcy-type flow in the porous medium to Navier-Stokes-type flow in the cracked medium [30]. One of the first attempts to simulate hydraulic fracturing was done by Boone and Ingraffea [11], where two-dimensional numerical approximations for poroelastic materials were considered. The FEM equations were solved using a partitioned solution procedure for poroelastic problems. Accounting for the continuous topological changes in the porous domain, Schrefler et al. [55] presented a dependency between the crack opening and the permeability in Darcy's flows. Secchi and Schrefler [56] and Cao et al. [17] simulated 3D hydraulic fracturing in fully saturated porous media using a cohesive fracture model. The model did not require a predefined fracture path, but needed a constant updating of mesh near the crack tip to consider geometry evolution. For incompressible viscous fluids, the fluid flow inside the crack was considered laminar and governed by the Poiseuille law as derived by Adler et al. [3]. Adachi et al. [2] added some modifications to the fluid flow equations, like a leak-off sink term, and presented controlling parameters for the crack growth evolution.

Significant contributions in the field of PFM were made by Miehe et al. [43] by relating the crack propagation only to the strain energy, where the evolution of the phase-field was related to a local history variable termed as the crack driving force. Extending this concept, Miehe et al. [46,42], Miehe and Mauthe [45] established a link between the diffusive crack modelling and the hydro-poro-elastic response of porous bulk materials. The energy-based crack driving force was further generalised to the solid effective stresses-based threshold criterion. A recent article by Heider and Markert [30] combined the TPM and PFM models to derive a more realistic hydraulic fracture model accounting for permanent local changes in the permeability and the volume fractions, while adopting the fluid velocity instead of the seepage velocity

as a primary variable to confer with the idea of changing flows from Darcy-type to Stokes-type in the cracked region. Additionally, Heider et al. [31] introduced an extended 3D study of the TPM-PFM approach that included a model calibration based on experimental data. Ehlers and Luo [25] have introduced a fully-coupled computational approach to simulate hydraulic fracturing in 2D and 3D settings by including the phase-field variable into the constitutive model for the solid and fluid phases, thus accounting for a direct influence of cracks on the solid deformations and the fluid velocities. Another approach involving PFM for hydraulic fracturing in porous media based on Biot's Theory has been investigated by Mikić et al. [48,49], Lee et al. [34] allowing them to implement advanced numerical schemes and explore different features of hydraulic fracturing.

The present work focuses on developing a fully-coupled computational framework for simulating dynamic hydraulic fracturing combining the TPM and PFM approaches via ABAQUS² UEL and UMAT subroutines. In this, in order to extend the existing fracture methodologies to deal with large-scale practical engineering problems involving a huge number of degrees of freedom, we use the robust multiphysics solving capabilities of ABAQUS involving parallel computing algorithms and automatic time-stepping schemes. Changes in the permeability, the volume fractions and the fluid flow behaviour during crack propagation are incorporated directly into the constitutive porous media model. Moreover, the present work discusses the procedure to model heterogeneities using a Python 2.7.6 script in conjunction with the ABAQUS input file to include initial material property variations based on the Weibull probability distribution, see Chen et al. [18] for details about the methodology. Numerical examples presented at the end of the paper show that the crack paths and fracture energies can significantly be affected when the heterogeneities are incorporated.

2. Theoretical background

2.1. Macroscopic porous media approach

Following the TPM for biphasic porous materials, the fluid and solid constituents are considered immiscible and ideally disarranged over a representative elementary volume (REV). The homogenisation of the REV yields a smeared-out continuum φ with overlapped solid and fluid constituents φ^α ($\alpha = S$ for the porous solid skeleton and $\alpha = F$ for the pore fluid), viz.

$$\varphi = \bigcup_{\alpha} \varphi^\alpha = \varphi^S \cup \varphi^F. \quad (1)$$

In view of immiscibility, the volume fractions $n^\alpha := dv^\alpha/dv$ can be defined as the local ratio of partial volume dv^α of constituent φ^α with respect to the total volume dv of the whole mixture φ . Within the context of a fully-saturated medium, no vacant spaces exist inside the matrix. As a direct consequence of this, the saturation relation $\sum_{\alpha} n^\alpha = n^S + n^F = 1$ also holds true, where n^S is the solidity and n^F is the porosity.

With the help of the volume fractions n^α , two different density functions for each constituent φ^α , the material density (effective or realistic) $\rho^{\alpha R} := dm^\alpha/dv^\alpha$ and partial density $\rho^\alpha := dm^\alpha/dv$ can be formulated, where dm^α and dv^α are the local mass and local volume elements, and dv is the aggregate volume element of the mixture. The fluid and solid effective densities (ρ^{SR}, ρ^{FR}) are assumed to be constant, where a constant temperature is considered. However, the material incompressibility of the individual constituents does not lead to bulk incompressibility, since the partial densities (ρ^S, ρ^F) and the overall mixture density can change due to altered volume fractions (n^S, n^F). Based on the TPM, the solid and fluid volume fractions should lie between 0 and 1, i.e. $0 < n^\alpha < 1$, and the fluid flow in interconnected pores is governed by Darcy or Forchheimer filter laws, see, e.g., [37].

² ABAQUS version 6.14 on Linux86 64.

However, during fracturing, the cracked region becomes fully filled up by the pore fluid and locally free of the solid phase, which implies $n^S = 0$ and $n^F = 1$. It is therefore advantageous to treat the free-flowing fluid in the cracked region by means of Stokes flow [30].

The fracture of the saturated porous body \mathcal{B} is characterised by an internal discontinuity Γ_c of the solid phase [37]. This can be modelled within the PFM as a diffusive crack using the phase-field variable $\phi^S(\mathbf{x}, t)$, which can further distinguish between the cracked state ($\phi^S = 1$) and intact state ($\phi^S = 0$) of the solid skeleton.

2.2. Kinematic relations

Considering a deformable continuum two-phase body, each spatial position vector \mathbf{x} of the current configuration is simultaneously occupied by particles ($\mathcal{P}^S, \mathcal{P}^F$) of the solid and fluid phases. Therefore, starting from different positions \mathbf{X}_α in the reference configuration, each constituent possesses an independent state of motion given by a Lagrangean (or material) motion function χ_α , velocity ($\dot{\chi}_\alpha$) and acceleration ($\ddot{\chi}_\alpha$) fields as

$$\begin{aligned} \mathbf{x} &= \chi_\alpha(\mathbf{X}_\alpha, t), \quad \dot{\chi}_\alpha = \frac{d}{dt}\chi_\alpha(\mathbf{X}_\alpha, t), \\ \ddot{\chi}_\alpha &= \frac{d^2}{dt^2}\chi_\alpha(\mathbf{X}_\alpha, t). \end{aligned} \quad (2)$$

The Eulerian (or spatial) description of the motion is obtained as $\mathbf{X}_\alpha = \chi_\alpha^{-1}(\mathbf{x}, t)$. An alternative representation of the velocity and acceleration fields is expressed in Eulerian settings as

$$\begin{aligned} \dot{\chi}_\alpha &= \dot{\chi}_\alpha(\mathbf{x}, t) = \mathbf{v}_\alpha(\mathbf{x}, t), \\ \ddot{\chi}_\alpha &= \ddot{\chi}_\alpha(\mathbf{x}, t) = (\mathbf{v}_\alpha)_\alpha' = \mathbf{a}_\alpha(\mathbf{x}, t). \end{aligned} \quad (3)$$

The material time derivatives for each individual component can be calculated as $(\cdot)_\alpha' = d_\alpha(\cdot)/dt = \partial(\cdot)/\partial t + \text{grad}(\cdot) \cdot \mathbf{v}_\alpha$, where (\cdot) is an arbitrary vector quantity. In multiphasic theories, the kinematic description of a fully saturated porous medium is described on the basis of Lagrangean setting for the solid skeleton using the solid displacement vector $\mathbf{u}_S := \mathbf{x} - \mathbf{X}_S$, whereas the motion of the pore-fluid can be either described on the basis of an Eulerian setting using the fluid velocity \mathbf{v}_F or by using a modified Eulerian setting via the seepage velocity $\mathbf{w}_F := \mathbf{v}_F - \mathbf{v}_S$ with $\mathbf{v}_S := (\mathbf{u}_S)_S'$. In the present formulation, \mathbf{v}_F is adopted as the primary variable to describe the pore fluid velocity instead of \mathbf{w}_F in order to account for the changing flow from Darcy type to Stokes type in the cracked region, since Darcy flow is applicable only for porous domains, see, e.g., [30]. In addition, two more primary variables, namely the pore-fluid pressure $p = p(\mathbf{x}, t)$ and the phase-field variable $\phi^S = \phi^S(\mathbf{x}, t)$, are considered in describing the coupled problem.

Following this, the solid deformation gradient tensor \mathbf{F}_S , the linearised Green-Lagrangean solid strain tensor $\boldsymbol{\varepsilon}_S$ and its spectral decomposition are expressed as

$$\begin{aligned} \mathbf{F}_S &= \text{Grad}_S \mathbf{x} = \mathbf{I} + \text{Grad}_S \mathbf{u}_S, \\ \boldsymbol{\varepsilon}_S &= \frac{1}{2}(\text{grad} \mathbf{u}_S + \text{grad}^T \mathbf{u}_S), \\ &= \sum_i \lambda_{Si} \mathbf{n}_{Si} \otimes \mathbf{n}_{Si} \quad \text{with } i = 1, 2, 3. \end{aligned} \quad (4)$$

Herein, λ_{Si} are the real eigenvalues and \mathbf{n}_{Si} are the eigenvectors of $\boldsymbol{\varepsilon}_S$ corresponding to λ_{Si} . It is assumed that the crack happens only during tension and not during compression, which makes it necessary to maintain the compressive resistance during crack closure [43,47]. To do this, the strain tensor is decomposed into positive (tensile) and negative (compressive) modes as

$$\boldsymbol{\varepsilon}_S = \boldsymbol{\varepsilon}_S^+ + \boldsymbol{\varepsilon}_S^- \quad \text{with } \boldsymbol{\varepsilon}_S^\pm = \sum_i \langle \lambda_{Si} \rangle^\pm \mathbf{n}_{Si} \otimes \mathbf{n}_{Si}, \quad (5)$$

where $\langle \lambda_{Si} \rangle^\pm := (\lambda_{Si} \pm |\lambda_{Si}|)/2$ are the Macaulay brackets leading to the positive and negative eigenvalues.

2.3. Extended TPM formulation

Following the works in, e.g., [25,30], the balance relations for the mixture (overall aggregate) and its constituents ($\alpha \in \{S, F\}$) can be written as follows:

- Mass balance relations:

$$\dot{\rho} + \rho \text{div } \dot{\mathbf{x}} = 0, \quad (\rho^\alpha)_\alpha' + \rho^\alpha \text{div } \dot{\chi}_\alpha = \hat{\rho}^\alpha. \quad (6)$$

- Momentum balance relations:

$$\rho \ddot{\mathbf{x}} = \text{div } \mathbf{T} + \rho \mathbf{b}, \quad \rho^\alpha \ddot{\chi}_\alpha = \text{div } \mathbf{T}^\alpha + \rho^\alpha \mathbf{b}^\alpha + \hat{\mathbf{p}}^\alpha. \quad (7)$$

Herein, ρ represents the mixture density, $\dot{\mathbf{x}}$ and $\ddot{\mathbf{x}}$ are the mixture velocity and acceleration, respectively, \mathbf{T}^α is the symmetric partial Cauchy stress tensor and $\mathbf{T} := \mathbf{T}^S + \mathbf{T}^F$. Moreover, \mathbf{b}^α denotes the partial mass-specific body force, where $\mathbf{b} = \mathbf{b}^S + \mathbf{b}^F$ is applied. $\hat{\rho}^\alpha$ is the mass production terms and $\hat{\mathbf{p}}^\alpha$ is the momentum production term. For simplicity, the underlying study proceeds with the following assumptions:

- (a) Dynamic fracturing: $\dot{\chi}_S = (\mathbf{v}_S)_S' \neq \mathbf{0}$; $(\mathbf{v}_F)_S' \neq \mathbf{0}$,
- (b) isothermal process,
- (c) body forces acting on the constituents are constant,
- (d) materially incompressible constituents,
- (e) no mass exchange between the constituents, $\hat{\rho}^\alpha = 0$.

Thus, the constituent balance relations, Eqs. (6)₂ and (7)₂ can be rewritten as:

- Partial mass balance \rightarrow Partial volume balance:

$$0 = (\rho^\alpha)_\alpha' + \rho^\alpha \text{div } \mathbf{v}_\alpha \rightarrow 0 = (n^\alpha)_\alpha' + n^\alpha \text{div } \mathbf{v}_\alpha. \quad (8)$$

- Partial momentum balance:

$$\rho^\alpha \ddot{\chi}_\alpha = \text{div } \mathbf{T}^\alpha + \rho^\alpha \mathbf{b} + \hat{\mathbf{p}}^\alpha. \quad (9)$$

The partial stress of each constituent in the fluid-saturated porous medium comprises of an effective stress term and a weighted pore pressure term, refer to [10,21]. Thus, having $\sigma^\alpha := \mathbf{T}^\alpha$ in the context of small strains, the effective stress and the effective momentum production terms are given by

$$\begin{aligned} \sigma_E^S &:= \sigma^S + n^S p \mathbf{I}, \quad \sigma_E^F := \sigma^F + n^F p \mathbf{I}, \\ \hat{\mathbf{p}}_E^F &:= \hat{\mathbf{p}}^F - p \text{grad } n^F. \end{aligned} \quad (10)$$

The equations for the terms σ_E^F and $\hat{\mathbf{p}}_E^F$ can further be formulated as:

$$\begin{aligned} \sigma_E^F &= n^F \mu^{FR} (\text{grad } \mathbf{v}_F + \text{grad}^T \mathbf{v}_F), \\ \hat{\mathbf{p}}_E^F &= -\frac{(n^F)^2}{K^F} \mathbf{w}_F, \end{aligned} \quad (11)$$

where σ_E^F is the fluid viscous stress tensor, K^F is the specific permeability, related to isotropic permeability properties, and μ^{FR} is the fluid dynamic viscosity.

The description of fluid flow within the porous medium is given in the context of Darcy's filter law [19], based on a simple linear fluid transport equation. Considering this, Eq. (11)₃ states that the interaction force term is linearly dependent on the seepage velocity, as described in [37]. However, the formulation in Eq. (11)₃ does not account for the change of the permeability K^F when the solid fractures. It is obvious that when the crack starts propagating, the permeability of the solid matrix starts to increase, as the crack width increases. To incorporate this effect, an exponential variation of the fluid permeability

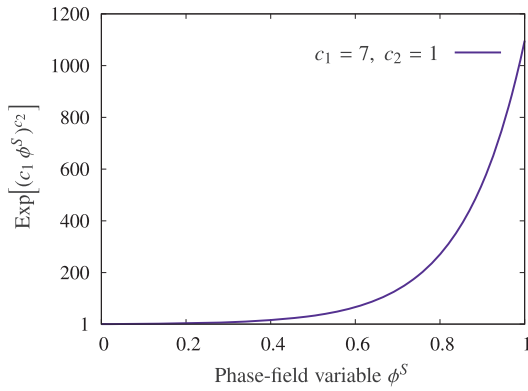


Fig. 1. Illustration of permeability increasing w.r.t the evolution of the phase-field variable.

has been proposed in [30,53], which starts from an initial value for a completely intact porous medium. The permeability can thus be expressed as a function of the phase-field variable as

$$K^F = \frac{k_0^F}{\gamma^{FR}} \text{Exp}[(c_1 \phi^S)^{c_2}], \quad (12)$$

which yields for the interaction force

$$\hat{\mathbf{p}}_E^F = \frac{-(n^F)^2 \gamma^{FR}}{k_0^F \text{Exp}[(c_1 \phi^S)^{c_2}]} \mathbf{w}_F \quad (13)$$

with k_0^F as the initial hydraulic conductivity and $\gamma^{FR} = \rho^{FR} |\mathbf{g}|$ represents fluid specific weight. The involved parameters c_1 and c_2 can be determined based on experimental data. In the numerical examples in this work, the values have been chosen as $c_1 = 7$ and $c_2 = 1$ (see, Fig. 1, for illustration). One can notice from Fig. 1 that for the intact state with $\phi^S = 0$, K^F has its initial value ($K_0^F = k_0^F / \gamma^{FR}$), whereas it increases exponentially and gains its maximum value at $\phi^S = 1$. In addition, the interaction force $\hat{\mathbf{p}}_E^F$ decreases as K^F increases. This is reasonable since the cracked region consists of only fluid phase, and $\hat{\mathbf{p}}_E^F$, accounting for the solid-fluid interaction, should vanish. However, for numerical stability purposes, a residual value of $|\hat{\mathbf{p}}_E^F|$ should be retained [30].

Since the cracked region consists only of the fluid phase, the solid volume fraction yields $n^S \rightarrow 0$ when $\phi^S \rightarrow 1$. In order to account for this effect during the propagation of the crack, an alternative formulation of n^S , that results from Eq. (8)₂, has been adopted, see [30]:

$$n^S = n_{0S}^S \det \mathbf{F}_S^{-1} \quad \text{with } n_{0S}^S = (1 - \phi^S) n_{0S}^S. \quad (14)$$

Here, n_{0S}^S is the initial solidity, and is recovered back for an undeformed ($\mathbf{F}_S = \mathbf{I}$) and an intact ($\phi^S = 0$) state.

The equation for the phase-field evolution $(\phi^S)'_S$, following the Allen-Cahn approach, can be expressed as:

$$(\phi^S)'_S = -\frac{1}{M} \left[\rho_0^S \frac{\partial \psi^S}{\partial \phi^S} - \text{div} \left(\rho_0^S \frac{\partial \psi^S}{\partial \text{grad } \phi^S} \right) \right], \quad (15)$$

where $M > 0$ denotes the crack mobility parameter. The mobility parameter controls the speed of crack formation, such that the pore fluid has enough time to fill the cracked domain, wherein increasing M leads to a lower crack speed and vice versa [30]. Within the limit $M \rightarrow 0$, Eq. (15) reduces to a rate-independent evolution equation. It can be noticed from Eq. (15) that the variations in the solid strain energy ψ^S lead to the evolution of the crack phase field. Fluid energy ψ^F does not appear in Eq. (15), since cracks exist only in the solid phase. However, in the case of hydraulic fracturing, the increase of ψ^S happens under the influence of increasing pore-fluid pressure due to fluid influx.

2.4. Energetic phase-field formulation

Within the energetic framework of brittle fracture of an isotropic,

elastic solid or porous body, the total potential energy \mathcal{F} is assumed to be the sum of the bulk strain energy and the crack surface energy. Thus, considering a body Ω with external boundary $\partial\Omega$ and internal discontinuous boundary Γ_c , and having G_c as the critical energy release rate, the total energy can be expressed as

$$\begin{aligned} \mathcal{F} &= \int_{\Omega \setminus \Gamma_c} \psi_{el}^S(\epsilon_S) d\Omega + \int_{\Gamma_c} G_c d\Gamma \\ &\approx \int_{\Omega} \psi^S(\epsilon_S, \phi^S, \text{grad } \phi^S) d\Omega. \end{aligned} \quad (16)$$

Herein, the phase-field variable $\phi^S(\mathbf{x}, t)$, bounded by the limits $\phi^S \in [0, 1]$, has been included to approximate the sharp crack interface by a diffusive one. Moreover, ψ_{el}^S comprises of deformation-dependent tensile (ψ_{el}^{S+}) and compressive (ψ_{el}^{S-}) parts. Thus, the solid strain energy density can be expressed as

$$\begin{aligned} \rho_0^S \psi^S(\epsilon_S, \phi^S, \text{grad } \phi^S) &= g(\phi^S) [\rho_0^S \psi_{el}^{S+}(\epsilon_S^+) + \rho_0^S \psi_{el}^{S-}(\epsilon_S^-)] \\ &\quad + G_c \gamma_c(\phi^S, \text{grad } \phi^S) \end{aligned} \quad (17)$$

with

$$\begin{aligned} g(\phi^S) &:= [(1 - \eta_S)(1 - \phi^S)^2 + \eta_S], \\ \rho_0^S \psi_{el}^{S+}(\epsilon_S^+) &= \mu^S (\epsilon_S^+ \cdot \epsilon_S^+) \\ &\quad + \frac{1}{2} \lambda^S \left(\frac{\text{tr}(\epsilon_S^+) + |\text{tr}(\epsilon_S^+)|}{2} \right)^2, \\ \rho_0^S \psi_{el}^{S-}(\epsilon_S^-) &= \mu^S (\epsilon_S^- \cdot \epsilon_S^-) \\ &\quad + \frac{1}{2} \lambda^S \left(\frac{\text{tr}(\epsilon_S^-) - |\text{tr}(\epsilon_S^-)|}{2} \right)^2, \\ \gamma_c(\phi^S, \text{grad } \phi^S) &= \frac{1}{2l_0} (\phi^S)^2 + \frac{l_0}{2} \text{grad } \phi^S \cdot \text{grad } \phi^S. \end{aligned} \quad (18)$$

In this, $g(\phi^S)$ is the stress-degradation function, while η_S is a small residual stiffness term that helps in better numerical convergence. The value of η_S should, however, be as small as possible and should not cause overestimation of the stresses. Moreover, λ^S and μ^S are Lamé constants and $\text{tr}(\epsilon_S)$ represents the trace of the strain tensor, where $\text{tr}(\epsilon_S) = \epsilon_S \cdot \mathbf{I} = \text{div } \mathbf{u}_S$. The crack in the solid matrix is assumed to occur only under tension and not compression. Therefore, the stress-degradation function $g(\phi^S)$ has only been multiplied with the positive energy ψ_{el}^{S+} [43]. The idea is to degrade the tensile stress to zero, when the material is fully-cracked ($\phi^S = 1$). Additionally, γ_c is the crack density function per unit volume [47] and l_0 is the length scale parameter controlling the diffusive crack topology, which in the limit $l_0 \rightarrow 0$ turns to a sharp crack. It should be noted that the parameter l_0 does not represent the actual crack width, but only denotes the amount by which the crack would be diffused into the surrounding domains. As suggested in [47], the length scale parameter should be chosen as small as possible, but should be at least twice of the minimum element size of the finite element mesh in the cracked domain for better approximation of the sharp crack edges.

Following this, the linearised effective solid stress tensor can be derived using Eq. (17) as

$$\begin{aligned} \sigma_E^S &= \rho_0^S \frac{\partial \psi^S}{\partial \epsilon_S} = g(\phi^S) \left[2\mu^S \epsilon_S^+ + \lambda^S \left(\frac{\text{tr}(\epsilon_S^+) + |\text{tr}(\epsilon_S^+)|}{2} \right) \mathbf{I} \right] + 2\mu^S \epsilon_S^- \\ &\quad + \lambda^S \left(\frac{\text{tr}(\epsilon_S^-) - |\text{tr}(\epsilon_S^-)|}{2} \right) \mathbf{I}. \end{aligned} \quad (19)$$

Furthermore, combining Eqs. (15), (17) and (18), the evolution equation of the phase field variable yields the form

$$(\phi^S)'_S = \frac{1}{M} \left[2(1 - \eta_S)(1 - \phi^S) \rho_0^S \psi_{el}^{S+} - G_c \left(\frac{\phi^S}{l_0} - l_0 \text{div } \text{grad } \phi^S \right) \right]. \quad (20)$$

In this connection, it is worth noting that Eq. (20) does not guarantee irreversibility of the cracking process during cyclic loading. A crack is a permanent damage and should not be capable of healing or recovering the stiffness. This can be accomplished by restricting the evolution of the phase-field variable such that

$$(\phi^S)'_S \geq 0. \quad (21)$$

To this end, based on [43], this can be ensured by introducing a local history variable of the maximum positive reference energy as

$$\mathcal{H} = \max_{t > t_0} (\rho_0^S \psi^{S+}), \quad (22)$$

which also acts as the crack driving force, determining the values of the phase-field variable ϕ^S . Therefore, the evolution Eq. (20) is rewritten in terms of the history variable \mathcal{H} . Moreover, in order to satisfy the constraint in Eq. (21) for crack irreversibility, $(\phi^S)'_S$ is set as

$$(\phi^S)'_S = \max \{(\phi^S)'_S, 0\}. \quad (23)$$

2.5. Governing partial differential equations

In summary, the applied governing partial differential equations (PDEs) to model the hydraulic fracturing problem read:

- Overall volume balance:

$$\text{div} (n^S \mathbf{v}_S + n^F \mathbf{v}_F) - \alpha \text{div} \text{grad} p = 0. \quad (24)$$

- Overall momentum balance:

$$\rho^S (\mathbf{v}_S)'_S + \rho^F (\mathbf{v}_F)'_F = \text{div} (\boldsymbol{\sigma}_E^S + \boldsymbol{\sigma}_E^F - p \mathbf{I}) + \rho \mathbf{b}. \quad (25)$$

- Fluid momentum balance:

$$\rho^F (\mathbf{v}_F)'_F = \text{div} \boldsymbol{\sigma}_E^F - n^F \text{grad} p + \rho^F \mathbf{b} - \hat{\mathbf{p}}_E^F. \quad (26)$$

- Phase-field evolution equation:

$$(\phi^S)'_S = \frac{1}{M} \left[2(1-\eta_S)(1-\phi^S) \mathcal{H} - G_c \left(\frac{\phi^S}{l_0} - l_0 \text{div} \text{grad} \phi^S \right) \right]. \quad (27)$$

Since the fluid is considered to be fully incompressible, the parameter α in Eq. (24) acts as a stabilising parameter, which is multiplied by the Laplacean term $\text{div} \text{grad} p$, refer to [30,54].

3. Numerical implementation

Based on the strong form of the governing Eqs. (24)–(27), the first step in the finite element treatment is the derivation of the corresponding weak form. In this, four primary variables are considered, which are the solid displacement \mathbf{u}_S , the fluid velocity \mathbf{v}_F , the pore-fluid pressure p and the phase-field variable ϕ^S . The strong form equations are weighted with independent test functions, based on the corresponding primary variables, and integrated over the spatial domain Ω of the overall body \mathcal{B} . Subsequently, the boundary terms are derived by applying product rules and the Gauss integral theorem to the integrands. In this, the boundary terms on $\Gamma = \partial\Omega$ have been split up into Dirichlet (essential) and Neumann (natural) boundaries, namely $\Gamma = \Gamma_p \cup \Gamma_v$ for the overall volume balance, $\Gamma = \Gamma_{u_S} \cup \Gamma_t$ for the overall momentum balance, $\Gamma = \Gamma_{v_F} \cup \Gamma_t^F$ for the fluid momentum balance and $\Gamma = \Gamma_{\phi^S} \cup \Gamma_c$ for the phase-field evolution equation. In summary, the weak formulation of the governing PDEs reads:

- Overall volume balance:

$$\begin{aligned} \mathcal{G}_p := & \int_{\Omega} \delta p \text{div} \mathbf{v}_S \text{dv} - \int_{\Omega} \text{grad} \delta p \cdot n^F \mathbf{w}_F \text{dv} + \alpha \int_{\Omega} \text{grad} \delta p \cdot \text{grad} p \text{dv} \\ & + \int_{\Gamma_v} \delta p \bar{v} \text{da} = 0. \end{aligned} \quad (28)$$

- Overall momentum balance:

$$\begin{aligned} \mathcal{G}_{u_S} := & \int_{\Omega} [\rho^S (\mathbf{v}_S)'_S + \rho^F (\mathbf{v}_F)'_S] \cdot \delta \mathbf{u}_S \text{dv} + \int_{\Omega} [\rho^F (\text{grad} \mathbf{v}_F) \mathbf{w}_F - \rho \mathbf{b}] \cdot \\ & \delta \mathbf{u}_S \text{dv} + \int_{\Omega} (\boldsymbol{\sigma}_E^S + \boldsymbol{\sigma}_E^F - p \mathbf{I}) \cdot \text{grad} \delta \mathbf{u}_S \text{dv} - \int_{\Gamma_t} \bar{\mathbf{t}} \cdot \delta \mathbf{u}_S \text{da} = 0. \end{aligned} \quad (29)$$

- Fluid momentum balance:

$$\begin{aligned} \mathcal{G}_{v_F} := & \int_{\Omega} \rho^F [(\mathbf{v}_F)'_S + (\text{grad} \mathbf{v}_F) \mathbf{w}_F] \cdot \delta \mathbf{v}_F \text{dv} + \int_{\Omega} (\boldsymbol{\sigma}_E^F - n^F p \mathbf{I}) \cdot \text{grad} \delta \mathbf{v}_F \text{dv} \\ & - \int_{\Omega} (p \text{grad} n^F + \rho^F \mathbf{b} + \hat{\mathbf{p}}_E^F) \cdot \delta \mathbf{v}_F \text{dv} - \int_{\Gamma_t^F} \bar{\mathbf{t}}^F \cdot \delta \mathbf{v}_F \text{da} = 0. \end{aligned} \quad (30)$$

- Phase-field evolution equation:

$$\begin{aligned} \mathcal{G}_{\phi^S} := & \int_{\Omega} [M (\phi^S)'_S - 2(1-\eta_S)(1-\phi^S) \mathcal{H}] \delta \phi^S \text{dv} \\ & + \int_{\Omega} \left(G_c \frac{\phi^S}{l_0} \delta \phi^S + G_c l_0 \text{grad} \phi^S \cdot \text{grad} \delta \phi^S \right) \text{dv} \\ & - \int_{\Gamma_c} G_c l_0 \text{grad} \phi^S \cdot \mathbf{n} \delta \phi^S \text{da} = 0. \end{aligned} \quad (31)$$

In the boundary integrals, \mathbf{n} is the outward-oriented unit surface normal, and $\bar{\mathbf{t}}$, $\bar{\mathbf{t}}^F$ and \bar{v} can be interpreted as the external mixture load vector, the external fluid load vector and the efflux of fluid mass, respectively. The expressions of the form of $\mathbf{n} \cdot \text{grad} \cdot$ represent the natural boundary condition for \cdot , and denote the way in which the system inside interacts with the system outside at the boundary. In particular, the boundary terms included in the weak-form equations read:

$$\begin{aligned} \bar{v} &= n^F (\mathbf{v}_F - \mathbf{v}_S) \cdot \mathbf{n}, \quad \bar{\mathbf{t}} = (\boldsymbol{\sigma}_E^S + \boldsymbol{\sigma}_E^F) \mathbf{n} - p \mathbf{n}, \\ \bar{\mathbf{t}}^F &= \boldsymbol{\sigma}_E^F \mathbf{n} - n^F p \mathbf{n}. \end{aligned} \quad (32)$$

These expressions for \bar{v} , $\bar{\mathbf{t}}$, $\bar{\mathbf{t}}^F$ yield non-zero values only if a Neumann condition is explicitly prescribed on a boundary surface. It is worth mentioning that at the boundary surface with normal \mathbf{n} , the condition $\text{grad} \phi^S \cdot \mathbf{n} = 0$ holds true, which makes the boundary integral in Eq. (31) to vanish.

3.1. Spatial discretisation

The continuous domain is discretised into finite dimensional elements, where the primary variables and the test functions are approximated over the discrete domain by use of trial and test functions as

$$\begin{aligned} \mathbf{u}(\mathbf{x}, t) &\approx \mathbf{u}^h(\mathbf{x}, t) = \bar{\mathbf{u}}^h(\mathbf{x}, t) + \sum_{i=1}^{N_u} \mathbf{N}_{u(i)}(\mathbf{x}) \mathbf{u}_{(i)}(t), \\ \delta \mathbf{u}^h(\mathbf{x}) &= \sum_{i=1}^{M_u} \mathbf{M}_{u(i)}(\mathbf{x}) \delta \mathbf{u}_{(i)}. \end{aligned} \quad (33)$$

In this, the primary variables are collected in a vector $\mathbf{u} := [\mathbf{u}_S \ p \ \mathbf{v}_F \ \phi^S]^T$, and the vector $\bar{\mathbf{u}}^h := [\bar{\mathbf{u}}_S^h \ \bar{p}^h \ \bar{\mathbf{v}}_F^h \ \bar{\phi}^h]^T$ defines the approximated Dirichlet boundary conditions. $\mathbf{N}_{u(i)}$ and $\mathbf{M}_{u(i)}$ represent the global basis functions at node i , which depend only on the spatial position \mathbf{x} , whereas the vectors $\mathbf{u}_{(i)}$ and $\delta \mathbf{u}_{(i)}$ denote the nodal values of the primary variables and their test functions. Moreover, N_u and M_u denote the number of FE nodes used for the approximation of the unknown field variables in \mathbf{u}^h and their test functions in $\delta \mathbf{u}^h$, respectively.

In the underlying treatment, a mixed finite element method has been used to avoid the ill-posedness arising due to the consideration of an incompressible pore fluid together with a monolithic time integration procedure, see [15,40,29,38] for references. Thus, in order to

satisfy the standard LBB criterion, discretisation is performed using quadrilateral Taylor-Hood elements with quadratic shape functions for the solid displacement \mathbf{u}_s , the solid-velocity \mathbf{v}_s and the fluid velocity \mathbf{v}_f , whereas linear shape functions are used for the pore pressure p and the phase-field variable ϕ^S .

3.2. Time discretisation

Several time-dependent quantities have been presented within the weak formulation Eqs. (28)–(31). These quantities have to be discretised in the time domain for calculation of the overall residual vector. In this, a monolithic-implicit time integration for the complete coupled problem is carried out using the backward Euler scheme. It is worth mentioning that when differential equations are volumetrically coupled with interaction terms in the governing equations, as in the current problem, a partitioned solution strategy of the porous media problem might not be computationally as efficient as a monolithic strategy [26,25]. The time-dependent variables like $(\mathbf{u}_s)_s$, $(\mathbf{v}_s)_s$, and $(\mathbf{v}_f)_s$ are provided directly inside ABAQUS UEL and, therefore, there is no need to calculate them explicitly.

3.3. Residual vector and stiffness matrix

A combined residual force vector for any $\{k + 1\}^{th}$ iteration can be formulated using the internal and external forces as follows:

$$\mathbf{r}(\mathbf{u}_k) = \mathbf{f}^{int}(\mathbf{u}_k) - \mathbf{f}^{ext}(\mathbf{u}_k). \quad (34)$$

Herein, \mathbf{f}^{int} and \mathbf{f}^{ext} are the internal and external force vectors, respectively, calculated from volume and surface integrals of the weak form equations. The volume and surface integrals are evaluated using the Gaussian quadrature rule. The idea is to seek a solution such that $\mathbf{r}(\mathbf{u}_{k+1}) \rightarrow \mathbf{0}$. Since the residual force is highly nonlinear in nature, an incremental iterative strategy has been adopted to solve the equations numerically using the Newton-Raphson method. The element stiffness matrix is given as the derivative of the residual vector with respect to the field variables \mathbf{u} :

$$\mathbf{K}(\mathbf{u}_k) = \frac{\partial \mathbf{r}}{\partial \mathbf{u}} \bigg|_{\mathbf{u}=\mathbf{u}_k} = \mathbf{K}^{int}(\mathbf{u}_k) - \mathbf{K}^{ext}(\mathbf{u}_k). \quad (35)$$

The external stiffness matrix yields $\mathbf{K}^{ext} = \mathbf{0}$ as the external force vector \mathbf{f}^{ext} consists of constant prescribed boundary values and does not depend on the primary variables in our treatment. Moreover, the internal stiffness matrix is calculated with the help of the numerical tangent method as

$$\mathbf{K}^{int} = \frac{\partial \mathbf{r}}{\partial \mathbf{u}} \bigg|_{\mathbf{u}=\mathbf{u}_k} \approx \frac{\mathbf{r}(\mathbf{u}_k + \epsilon) - \mathbf{r}(\mathbf{u}_k)}{\epsilon}, \quad (36)$$

where ϵ represents a very small perturbation vector of the field variables \mathbf{u}_k .

4. ABAQUS implementation

The combined TPM and PFM model is implemented into ABAQUS via a user element (UEL) subroutine. The methodology to incorporate the phase-field method to model hydraulic fracturing into the UEL is based on [51]. However, utilisation of a UEL poses additional challenges related to the implementation of the coupled Neumann boundary conditions on the external surfaces and visualisation of the primary variables, which are not inherently supported by ABAQUS. Prescription of distributed loads requires the definition of a surface comprising element's boundary faces. As the element topology is hidden inside the UEL subroutine and is unknown to ABAQUS pre-processor, it does not allow the creation of a boundary surface out of user-defined elements. However, this can be addressed by defining sets (ELSET) of boundary elements in the input file and passing the

information of their boundary face IDs to the UEL subroutine via the load-type key in *DLOAD, so that the surface integrals, present in the weak formulations, can be resolved. Moreover, post-processing of UEL results using standard tools like ABAQUS/Viewer can be a cumbersome task, specially if one wants to visualise quantities calculated on Gauss integration points instead of elemental nodes. This is because the ABAQUS library does not contain information about the user-defined shape functions used in the UEL, and, hence, cannot automatically extrapolate results from Gauss points to the element nodes. There are primarily two ways to solve this problem, see also [51]. One way is to write a script for accessing the ABAQUS output database (.odb) file, extracting results from Gauss points and recalculating them as nodal values, which can be displayed using external post-processors like Tecplot, Paraview, etc. Alternatively, a dummy mesh consisting of standard ABAQUS elements with known element types and shape functions can be used, which is superimposed over the actual mesh with user-elements. The results from the UEL can be stored in state-dependent variables (SDV) and transferred on to the dummy mesh using Fortran COMMON blocks and a UMAT subroutine containing definition of the complete constitutive behaviour of a dummy material.

The dummy or fictitious mesh matches the original mesh exactly and consists of duplicate elements interconnected with user-elements at common nodes. It should be noted that the material parameters, like elasticity modulus, chosen for the dummy mesh, should be as small as possible, so that they do not create any resistance to the original strains. In accordance, the Young's modulus for the dummy mesh is set close to machine precision ($\sim 10^{-15}$). Furthermore for the dummy mesh, CPE4 and CPE8RP elements from the Abaqus standard library have been chosen for solid and fluid-saturated porous materials, respectively. However, care must be taken while selecting the dummy element types, such that no mismatch between the element topology and formulations of the dummy mesh and the actual mesh occurs [51].

The state variables SVARS calculated in the UEL subroutine are transferred to the UMAT via COMMON blocks and stored in the STATEV array, so that they can be accessed directly for visualisation purpose. Furthermore, for the current nonlinear analysis, *Static, Implicit* analysis has been chosen for the pure solid case and *Soils, Consolidation* analysis for porous media, wherein the latter involves inclusion of transient dynamic effects. While there is no restriction on the time-step chosen for *Static, Implicit* analysis, spurious oscillations might occur if the time-step sizes are extremely small for transient consolidation analysis of fully saturated flows. Thus, if the analysis requires very small time-step sizes, a finer mesh is required to be implemented.

An illustration depicting the communication between the ABAQUS solver and the UEL/UMAT subroutines is shown in Fig. 2.

5. Weibull distribution

Materials like ceramics, glass, or rocks show inherent heterogeneity due to the presence of randomly-oriented micro-structural cracks or a random pore distribution. This can influence the crack behaviour, including variations in the crack path and the fracture driving force [18]. The Weibull distribution, which is commonly used to predict the distribution of the strength reliability, has been incorporated into the model definition in the current work to give meaningful insight into crack propagation patterns in heterogeneous materials. Using a two-parameter Weibull model, discrete values of a scalar-valued variable x (e.g. Young's modulus E , crack resistance G_c or solid volume fraction n^S) centred around a mean value can be obtained, where each value corresponds to a particular probability of occurrence. This probability further determines the total number of the elements in the FE model, to which this parameter value should be assigned. Ultimately, following the Weibull distribution, one obtains a completely heterogeneous model consisting of multiple element sets, to each a distinct value of the parameter x is assigned.

The probability density function (PDF) and the cumulative density

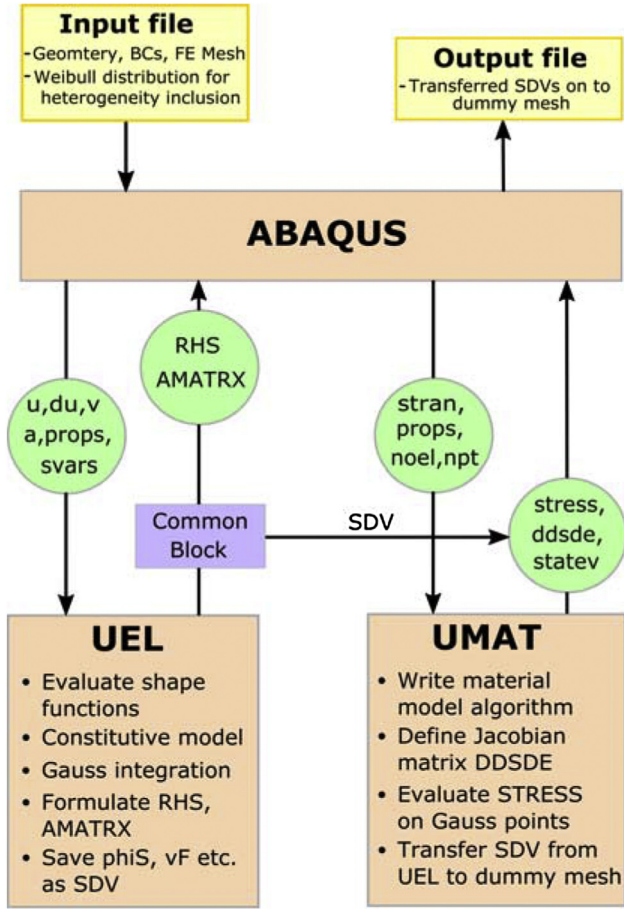


Fig. 2. Flow-chart illustrating the interaction of the ABAQUS solver with the UEL and UMAT subroutines.

function (CDF) for a two-parameter Weibull distribution are expressed as

$$\begin{aligned} \text{PDF: } f(x; a, b) &= \frac{a}{b} \left(\frac{x}{b}\right)^{a-1} e^{-(x/b)^a}; x \geq 0, \\ \text{CDF: } F(x; a, b) &= 1 - e^{-(x/b)^a}. \end{aligned} \quad (37)$$

Herein, $a > 0$ is the shape parameter (Weibull modulus) denoting the heterogeneity index of the distribution, and $b > 0$ is the scale parameter, which defines the amount by which the given distribution is spread out. The scale parameter b can be expressed in terms of the mean value μ_x of the variable x and the Gamma function as follows, see [18]:

$$b = \frac{\mu_x}{\Gamma\left(1 + \frac{1}{a}\right)}. \quad (38)$$

As an example, consider the heterogeneous distribution of the Young's modulus E with a mean value $\mu_E = 210$ GPa and Weibull shape parameter $a = 2.0$, which leads to PDF and CDF taking the form as shown in Fig. 3. It can be seen that the probability density function tends to 0 for very small and very large values of the Young's modulus, and most of the values generated lie around the mean value μ_E . In order to extract n discrete E values from the distribution, we adopt the following reformulation of Eq. (37)₂:

$$E_i = b \left[\ln\left(\frac{1}{1-F(E_i)}\right) \right]^{\frac{1}{a}}; i \in n. \quad (39)$$

From the continuous Weibull distribution function, the discrete probability of occurrence $P(E_i)$ for each E_i can be obtained as

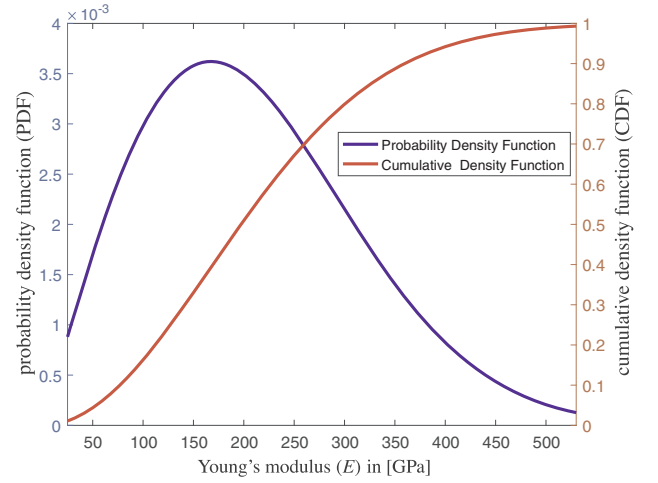


Fig. 3. Weibull PDF and CDF defined for Young's modulus (E).

$$P(E_i) = \frac{F(E_{i+1}) - F(E_i)}{2} + \frac{F(E_i) - F(E_{i-1}))}{2}, \quad (40)$$

where $F(E_i) = 0$ for $i < 0$ and $F(E_i) = 1$ for $i > n$. Each element in the FE model is then picked up randomly and is assigned with one of the Young's modulus values E_i . The elements assigned with a particular E_i form a common element set and the size of this set should be consistent with its corresponding probability $P(E_i)$. For example, if the probability for $E = 200$ GPa is 0.2, this means that 20% of the total elements present in FE model should be assigned with $E = 200$ GPa with a random spatial distribution. For illustration, Fig. 4 shows a transformation from a homogeneous to a heterogeneous spatial distribution of a variable x , applied in connection with the FE mesh of the ABAQUS input model.

6. Numerical examples

6.1. Homogeneous solid under mode-I fracture

In this section, the finite element method (FEM) is applied for the numerical solution of a 2D plane-strain boundary-value problem (BVP), as was considered in [47]. The dimensions and boundary conditions are shown in Fig. 5(a), while the material parameters are given in Table 1. A horizontal notch is modelled as an actual feature of the geometry and is placed at the middle height spanning from the domain's centre to its left edge. The mesh is refined in the areas where the crack is expected to propagate, see Fig. 5(b), with an effective element size of $h \approx 0.005$ mm in the central strip extending from the tip of the notch to the right end of domain.

The bottom edge is completely fixed in vertical and horizontal directions, whereas the nodes of the top edge are also constrained in the horizontal direction. A monotonic displacement load of $\bar{u} = 0.01$ mm is applied on the top edge with **AMPLITUDE = RAMP** option in ABAQUS and the analysis is carried out until the crack fully propagates. The crack initiates at $\bar{u} = 0.005598$ mm for the given material parameters

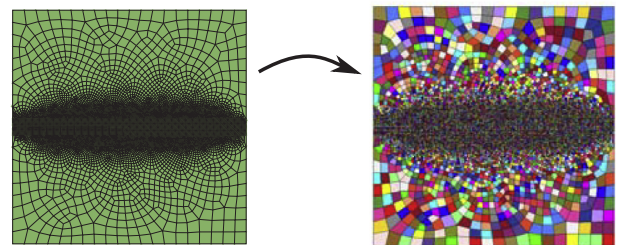


Fig. 4. Transformation from a spatially-uniform (homogeneous) to a statistically randomised (heterogeneous) Young's modulus via Weibull distribution.

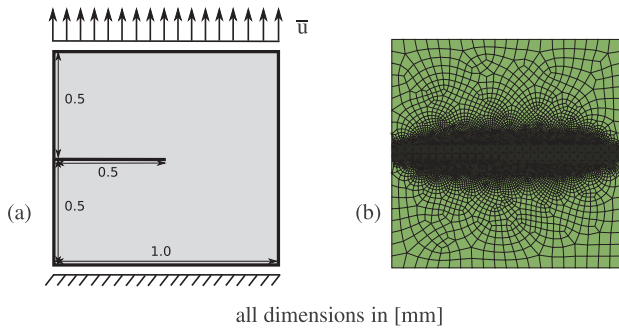


Fig. 5. (a) Geometry and boundary conditions of the homogeneous square pure-solid BVP, (b) finite element mesh.

Table 1

Model parameters for the solid square BVP [47].

Parameters	Symbol	Value	Unit
Young's modulus	E	210	GPa
Poisson's ratio	ν	0.3	–
Length scale	l_0	0.015	mm
Crack resistance	G_c	2.7×10^{-3}	kN/mm
Residual stiffness	η_S	1.0×10^{-5}	–

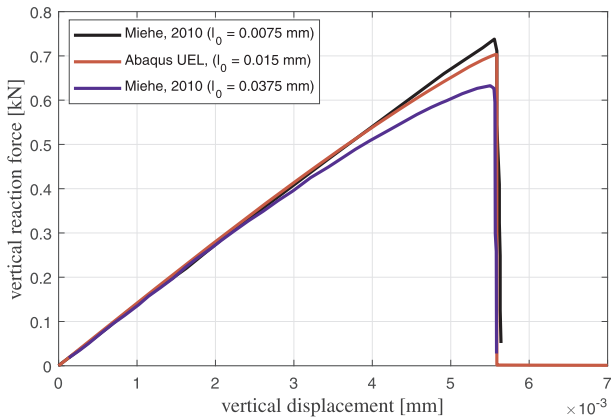


Fig. 6. Force vs. displacement in the vertical direction for the homogeneous solid BVP under mode-I fracture, compared to the results from Miehe et al. [47].

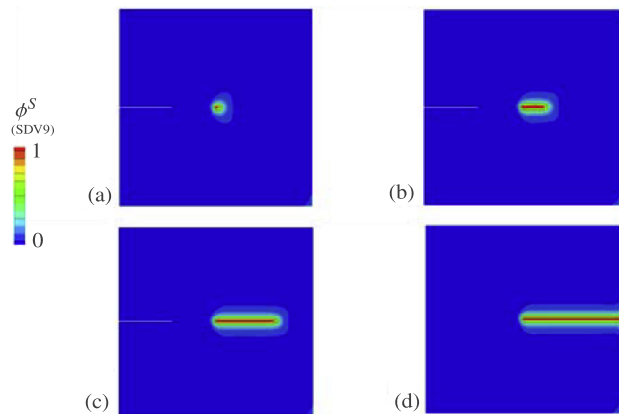


Fig. 7. Crack propagation pattern for the homogeneous solid BVP at successive time steps $t_a > t_b > t_c > t_d$.

and is accompanied with a sharp decline of the vertical reaction force, see Fig. 6. The sharp drop in the reaction force is justified considering the brittle nature of the fracture with no plasticity defined. The crack

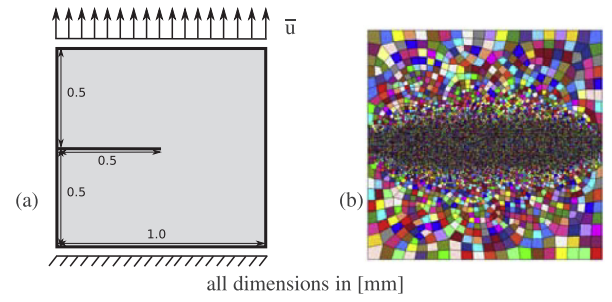


Fig. 8. (a) Geometry and boundary conditions, and (b) FE mesh for the pure tension test in the heterogeneous E case.

propagation at various time-steps is shown in Fig. 7, wherein the propagation is linear and perpendicular to the applied load. On the contrary, the crack paths can significantly change in case of heterogeneous materials leading to a change in the maximum force required for fracture and will be discussed in the subsequent section. Our results are consistent with the ones present in the related literature, see [47], from where the material parameters have been adopted. A slight deviation from [47] can, however, be observed due to the use of a different length scale parameter as well as different finite element types (quadrilateral instead of triangular).

6.2. Heterogeneous solid under mode-I fracture

As has been shown in Fig. 7, for a 2D square solid BVP with homogeneous material properties, the crack propagates straight and exactly perpendicular to the direction of the applied load. This is, however, not the case when a heterogeneous distribution of material properties is considered. The crack propagation, by principle, proceeds towards the elements, which have lesser stiffness and are more susceptible towards cracking. The heterogeneous model with statistically varying Young's modulus E (illustrated in Fig. 8) has been generated by using the two-parameter Weibull distribution function. This creates a combination of low and high stiffness elements in the entire model including the central strip, where the crack is expected to propagate. This leads in turn to a heterogeneous distribution of the crack driving force as it is a function of the elasticity modulus. For the comparison, different degrees of randomisation, i.e. $n = 50$, $n = 100$ and $n = 300$ are examined to generate the heterogeneous distribution, see Eq. (39). Additionally, two values of the mean Young's modulus are tested, namely, $\mu_E = 210$ GPa and $\mu_E = 240$ GPa. The other material, mesh and analysis parameters indicated in Table 1 and Section 6.1 have been kept unchanged, while $\alpha = 2.0$ has been chosen.

Fig. 9 presents the crack trajectory for the heterogeneous sample at

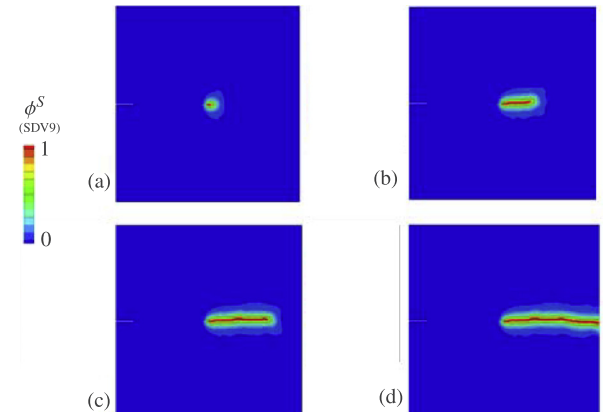


Fig. 9. Mode-I crack propagation pattern for the heterogeneous solid under tension at successive time steps $t_a > t_b > t_c > t_d$.

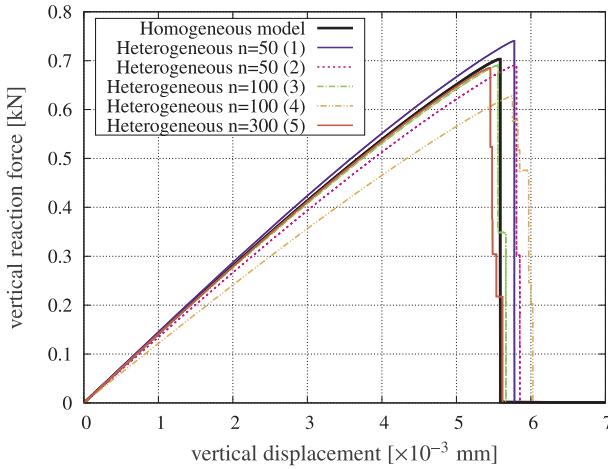


Fig. 10. Comparison of the force-displacement curves for the BVP between the homogeneous case and different heterogeneous cases; Case (1) $n = 50$, $\mu_E = 240$ GPa. Case (2) $n = 50$, $\mu_E = 240$ GPa (different pattern of heterogeneity than (1)). Case (3) $n = 100$, $\mu_E = 240$ GPa. Case (4) $n = 100$, $\mu_E = 210$ GPa. Case (5) $n = 300$, $\mu_E = 240$ GPa.

different time steps. Comparing it to the pure homogeneous case in Fig. 7, it can be seen that the crack adopts a curvy path searching for elements with lesser stiffness ahead of the crack-tip.

The force-displacement curves for different values of n and Young's modulus mean values μ_E are shown in Fig. 10 and compared to the original homogeneous case.

It can be seen that if the mean Young's modulus μ_E for the heterogeneous model randomised via Weibull distribution is chosen equal to that of Young's modulus E of the homogeneous model, as in case (4) $n = 100$, $\mu_E = 210$ GPa, the resulting heterogeneous model always leads to a softer response, i.e. displays lower elastic stiffness and peak fracture forces. This phenomena can be explained considering a simpler one-dimensional model with two elements, where μ_E represents an arithmetic mean of the Young's moduli in the Weibull distribution.³ In order to obtain a similar global elastic response (comparable force-displacement curves), the mean Young's modulus of the heterogeneous case should always be chosen higher than the homogeneous one. It has been chosen in this example $\mu_E = 240$ GPa, whereas different values of n have been tested. Moreover, the plots display that with increasing randomisation n of the material property E , the force-displacement curves become closer to the homogeneous case.

6.3. Hydraulic fracturing in homogeneous porous media

The numerical example in this section simulates hydraulic fracturing of a fully-saturated porous specimen under the influence of increasing pore-fluid pressure along a centrally placed fluid filled notch. The model parameters and boundary conditions for the initial boundary-value problem (IBVP) have been mostly adopted from [25,30]. The geometry and boundary conditions of the IBVP are illustrated in Fig. 11.

Owing to the symmetry of the problem, only the right-half of model has been analysed with appropriate boundary conditions. The mesh is refined with an effective element size $h \approx 0.004$ m in the central horizontal strip similar to the case considered in Fig. 4. A horizontal notch

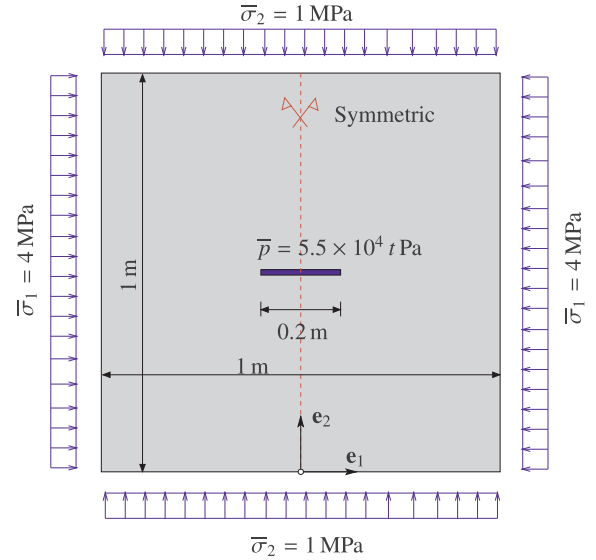


Fig. 11. Geometry and boundary conditions of the IBVP of hydraulic fracturing with a notch in the centre, where all the external boundaries are drained ($\bar{p} = 0$).

Table 2
TPM and PFM parameters [25].

Parameters		Value	Unit
1st Lamé parameter	λ^S	1.21×10^{11}	Pa
2nd Lamé parameter	μ^S	8.077×10^{10}	Pa
Length scale	l_0	4×10^{-3}	m
Crack resistance	G_c	2.7×10^3	N/m
Residual stiffness	η_S	1.0×10^{-4}	–
Crack mobility	M	3×10^3	N s/m ²
Eff. dyn. fluid viscosity	μ^F	1.002×10^{-3}	Pa/s
Initial solidity	n_{0S}^S	0.8	–
Init. Darcy permeability	k_0^F	1.0×10^{-8}	m/s
Effective solid density	ρ_0^{SR}	3.0×10^3	kg/m ³
Effective fluid density	ρ^{FR}	1.0×10^3	kg/m ³

of width 0.002 m and length 0.1 m is placed at the middle height of the specimen. The material parameters can be obtained from Table 2.

The distributed loads are applied at the top, bottom and right boundaries as illustrated in Fig. 11, which serve as confining stresses $\bar{\sigma}_1$ and $\bar{\sigma}_2$ for the solid skeleton. At the symmetry edge, the solid displacement and fluid velocity components normal to the edge vanish, i.e. $\bar{u}_{S1} = 0$ and $\bar{v}_{F1} = 0$ (impermeable). The remaining boundaries are treated as fully permeable, where the pore-fluid pressure is prescribed as zero ($\bar{p} = 0$). The loading at the notch is given as an increasing pore pressure of $\bar{p} = 5.5 \times 10^4$ t Pa within transient dynamic *SOILS, CONSOLIDATION analysis available in ABAQUS, whereas the confining stresses and pore pressure at the boundary are kept constant. It is worth mentioning that the application of confining stresses as distributed loads is not directly supported for ABAQUS user elements and has been facilitated within the UEL subroutine.

Since the analysis is transient and extremely small time increments may lead to spurious oscillations of the solution [1], a minimum time step size of 10^{-6} s is specified. The prescribed pore pressure leads to hydraulic cracking of the specimen, refer to Fig. 12. The crack propagates perpendicular to the notch and is normal to the maximum stress $\bar{\sigma}_1$ at the boundary ($\bar{\sigma}_1 > \bar{\sigma}_2$), which is consistent with the plane-strain hydraulic fracture cases considered in [35,39,57,30].

Fig. 13 depicts the change in magnitude of the resultant fluid velocities as the crack propagates. It can be seen that when the solid skeleton cracks, the pore fluid rushes into the cracked cavity, with an

³ Consider a simple 1-D model with two linear-elastic elements that have the same length l and cross section A , but different (heterogeneous) elasticity moduli, i.e. E_1 and E_2 . Applying an axial load F leads to an elongation of $\Delta l = (\frac{1}{E_1} + \frac{1}{E_2}) \frac{F l}{A}$. For the homogeneous case with one elasticity modulus E , the same elongation is obtained if $\frac{1}{E_1} + \frac{1}{E_2} = \frac{2}{E}$ (harmonic mean). Instead, if the arithmetic mean is used for the homogeneous case, i.e. $\bar{E} := \frac{(E_1 + E_2)}{2}$, then this leads to a different elongation as $E < \bar{E}$.

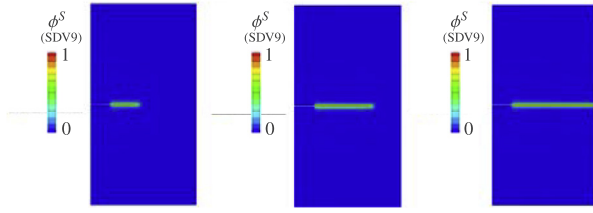


Fig. 12. Hydraulic crack propagation in the homogeneous porous media domain.

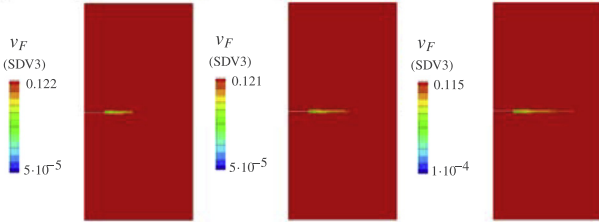


Fig. 13. Contour plots of the resultant norm of the fluid velocity vector v_F [m/s] during crack propagation for a homogeneous porous specimen.

increased fluid velocity.

The pore pressure distribution at the onset of the crack is shown in Fig. 14, with the crack initiating at around $\bar{p} = 56$ MPa.

After onset of the fracture, it is assumed that there is no solid constituent inside the cracked domain. Thus, the fluid permeability should rise to a very high value as $\phi^S \rightarrow 1$. As a direct consequence, the fluid should rush with a high velocity into the cracked cavity and results in an increase of the fluid pressure. Given that in the present example, the permeability inside the crack increases only by around 1000 times the original permeability, the pore pressure does not rise significantly in comparison to the applied pressure at the notch. This can however, be achieved by testing different combinations of c_1 and c_2 in Eq. (12), resulting in a higher increase of the permeability as the crack propagates (see also [31] for a thorough discussion about the flow in the crack). The mobility parameter M also plays a vital role in making the crack propagate slow enough to allow the fluid to fill the cracked region, and thus increasing the pressure inside the cavity.

6.4. Hydraulic fracturing in heterogeneous porous media

To perform a comparative study between hydraulic crack propagation patterns in homogeneous and heterogeneous cases, we consider a model problem similar to the one described in Section 6.3, but without a predefined notch. All model parameters (Table 2) and the boundary conditions (Fig. 11) remain exactly the same as described in Section 6.3. However, in the present case, the pore-fluid pressure is increased linearly at a small boundary segment, located exactly at the centre of the sample (Fig. 15). Under the assumption of an inherent

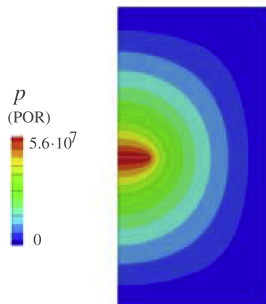


Fig. 14. Pore-pressure contour plot (p in [MPa]) at the onset of the crack for a homogeneous porous specimen.

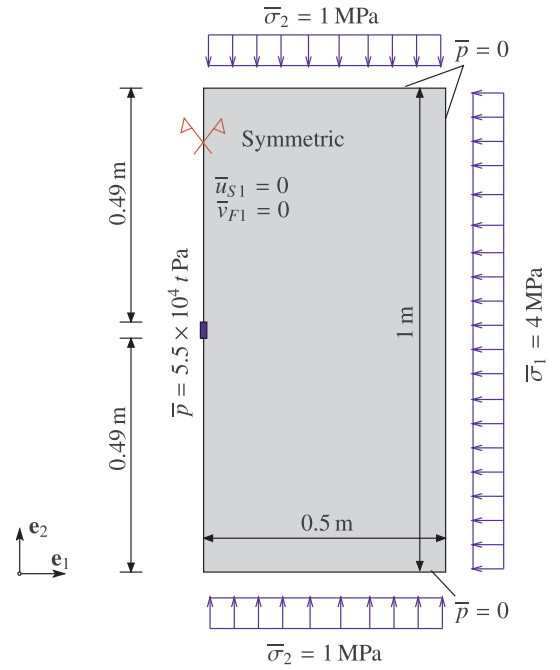


Fig. 15. Geometry and boundary conditions for the IBVP of hydraulic fracturing.

symmetric material micro-structure, the domain in the heterogeneous case is also considered symmetric and half of the model has been analysed. As seen in the previous section, the crack propagated exactly perpendicular to the maximum applied stress at the boundary for the homogeneous case, whereas for the heterogeneous case, it might take an arbitrary path depending on the element stiffness ahead of the crack tip as was seen in the case of a heterogeneous pure solid model in Section 6.2.

For the heterogeneous case of hydraulic fracturing, the statistical variation based on the Weibull distribution can be created for a number of different properties, including Young's modulus E , crack resistance G_c , Poisson's ratio ν , etc. For the sake of comparison of crack patterns, the present study only considers a variation of Young's modulus E based on the Weibull distribution with a total of 50 distinct values (i.e. degree of randomisation $n = 50$) over the entire domain. The parameters required for creating the Weibull distribution of E can be taken from Section 6.2, wherein a mean value of $E = 210$ GPa and Weibull modulus $a = 2.0$ are considered.

The difference between crack propagation patterns in the homogeneous and the heterogeneous cases can be seen in Fig. 16, (a) and (b). As expected, the crack propagates exactly horizontal and perpendicular to the maximum stress ($\bar{\sigma}_1 = 4$ MPa) in case of the homogeneous sample. However, in the heterogeneous case, the crack topology significantly deviates from the horizontal path and propagates in somewhat curvilinear fashion searching for elements with minimum stiffness ahead of the crack tip. An additional crack branching can be seen, which happens because the crack energy cannot be dissipated now with a single crack due to the presence of higher-stiffness elements in the crack path.

7. Conclusions

In this work, an approach to simulate brittle fractures in homogeneous and heterogeneous solids and porous materials, and the corresponding implementation of the multi-field problem using ABAQUS subroutines has been presented. The phase-field model (PFM), embedded into the continuum mechanical Theory of Porous Media (TPM), has been implemented into user-element subroutines (UEL) for the

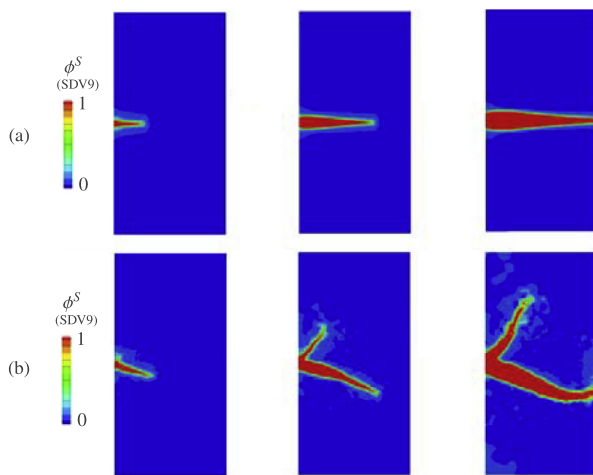


Fig. 16. Comparison of crack topology during crack propagation for (a) homogeneous and (b) heterogeneous case.

numerical modelling of crack propagation in biphasic, incompressible porous media. A procedure has also been introduced to incorporate heterogeneities arising due to material microstructure and random pore arrangement into the ABAQUS input definition by means of the Weibull distribution. The numerical model has been qualitatively verified by simulating crack propagation in pure solids as well as porous materials. Furthermore, a comparison has been made between the crack propagation behaviour in homogeneous and heterogeneous materials, where the latter assumes property variation based on the Weibull model. The evolution of the phase-field variable during crack propagation causes permanent changes in the volume fractions and fluid permeability, which have also been accounted in the current work. Solving coupled porous media fracture problems in ABAQUS poses additional problems with the definition of natural boundary conditions, since ABAQUS does not allow a direct definition of boundary surfaces for user-defined elements. The problem has been addressed and solved within the UEL subroutine by passing appropriate information from the input file. In hydraulic fracturing, the crack propagates perpendicular to the maximum confining stress at the boundary, and also the resultant fluid velocity increases in the cracked-cavity upon occurrence of the crack, which is in good agreement with the literature. The numerical examples presented in this paper show that the crack path significantly deviates when the heterogeneous nature of the material is considered. The crack adopts an arbitrary curvilinear topology searching for elements with lesser stiffness ahead of the crack tip. It should be noted however, that with the same degree of randomisation, different patterns of heterogeneities can be created within the same model, and in each case, the crack would follow a different path.

The present work can be considered as an introduction to a methodology, which creates initial material property variations based on the Weibull distribution and also couples it with ABAQUS user subroutines to understand the crack propagation behaviour when heterogeneities are incorporated. For accurate prediction of crack paths in heterogeneous materials, Monte-Carlo simulations must be performed to determine the most probable outcome for crack topology. Moreover, the implementation of the model in ABAQUS UEL can be extended to consider 3D geometries and boundary conditions in order to get more realistic and scalable results.

acknowledgements

The author, Udit Pillai, would like to acknowledge that the work on this manuscript has been carried out during his research stay at the Institute of General Mechanics, RWTH Aachen University

References

- [1] ABAQUS, V6.14 Documentation, ABAQUS Inc., Dassault Systèmes Simulia Corp., Providence, RI, USA, 2014.
- [2] J. Adachi, E. Siebrits, A. Peirce, J. Desroches, Computer simulation of hydraulic fractures, *Int. J. Rock Mech. Min. Sci.* 44 (5) (2007) 739–757.
- [3] P.M. Adler, J.-F. Thovert, V.V. Mourzenko, *Fractured Porous Media*, Oxford University Press, 2013.
- [4] F. Aldakheel, P. Wriggers, C. Miehe, A modified gurson-type plasticity model at finite strains: formulation, numerical analysis and phase-field coupling, *Comput. Mech.* (2017) <http://dx.doi.org/10.1007/s00466-017-1530-0>.
- [5] M. Ambati, T. Gerasimov, L.D. Lorenzis, A review on phase-field models of brittle fracture and a new fast hybrid formulation, *Comput. Mech.* 55 (2015) 383–405.
- [6] T. Belytschko, T. Black, Elastic crack growth in finite elements with minimal re-meshing, *Int. J. Numer. Meth. Eng.* 45 (5) (1999) 601–620.
- [7] M.A. Biot, General theory of three-dimensional consolidation, *J. Appl. Phys.* 12 (2) (1941) 155–164.
- [8] M.A. Biot, Theory of propagation of elastic waves in a fluid-saturated porous solid. I. Low-frequency range, *J. Acoust. Soc. Am.* 28 (2) (1956) 168–178.
- [9] M.A. Biot, Theory of propagation of elastic waves in a fluid-saturated porous solid. II. Higher frequency range, *J. Acoust. Soc. Am.* 28 (2) (1956) 179–191.
- [10] A. Bishop, The effective stress principle, *Teknisk Ukeblad* 39 (1959) 859–863.
- [11] T.J. Boone, A.R. Ingraffea, A numerical procedure for simulation of hydraulically-driven fracture propagation in poroelastic media, *Int. J. Numer. Anal. Methods Geomech.* 14 (1) (1990) 27–47.
- [12] B. Bourdin, G.A. Francfort, J.-J. Marigo, Numerical experiments in revisited brittle fracture, *J. Mech. Phys. Solids* 48 (4) (2000) 797–826.
- [13] R.M. Bowen, Incompressible porous media models by use of the theory of mixtures, *Int. J. Eng. Sci.* 18 (9) (1980) 1129–1148.
- [14] R.M. Bowen, Compressible porous media models by use of the theory of mixtures, *Int. J. Eng. Sci.* 20 (6) (1982) 697–735.
- [15] F. Brezzi, M. Fortin, *Mixed and Hybrid Finite Element Methods* vol. 15, Springer Science & Business Media, 2012.
- [16] T. Cajuhi, L. Sanavia, L. De Lorenzis, Phase-field modeling of fracture in variably saturated porous media, *Comput. Mech.* (2017), <http://dx.doi.org/10.1007/s00466-017-1459-3>.
- [17] T.D. Cao, F. Hussain, B.A. Schrefler, Porous media fracturing dynamics: stepwise crack advancement and fluid pressure oscillations, *J. Mech. Phys. Solids* 111 (2018) 113–133.
- [18] Y. Chen, S. Sun, Y. Liu, Numerical simulation of the mechanical properties and failure of heterogeneous elasto-plastic materials, *Tsinghua Sci. Technol.* 12 (5) (2007) 527–532.
- [19] H. Darcy, *Les fontaines publiques de la ville de Dijon: exposition et application...* Victor Dalmont, 1856.
- [20] R. De Boer, Highlights in the historical development of the porous media theory: toward a consistent macroscopic theory, *Appl. Mech. Rev.* 49 (1996) 201–262.
- [21] R. De Boer, W. Ehlers, The development of the concept of effective stresses, *Acta Mech.* 83 (1–2) (1990) 77–92.
- [22] W. Ehlers, On thermodynamics of elasto-plastic porous media, *Arch. Mech.* 41 (1) (1989) 73–93.
- [23] W. Ehlers, *Poröse Medien – ein kontinuumsmechanisches Modell auf der Basis der Mischungstheorie*, Forschungsberichte aus dem Fachbereich Bauwesen, Heft 47, Universität-GH-Essen, 1989.
- [24] W. Ehlers, Constitutive equations for granular materials in geomechanical context, in: K. Hutter (Ed.), *Continuum Mechanics in Environmental Sciences and Geophysics*. CISM Courses and Lectures No. 337, Springer-Verlag, Wien, 1993, pp. 313–402.
- [25] W. Ehlers, C. Luo, A phase-field approach embedded in the theory of porous media for the description of dynamic hydraulic fracturing, *Comput. Methods Appl. Mech. Engrg.* 315 (2017) 348–368.
- [26] C. Felippa, K. Park, Synthesis tools for structural dynamics and partitioned analysis of coupled systems, in: A. Ibrahimbegovic, B. Brank (Eds.), *Engineering Structures Under Extreme Conditions: Multi-physics and Multi-scale Computer Models in Non-linear Analysis and Optimal Design*, ISO Press, 2005, pp. 50–111.
- [27] G.A. Francfort, J.-J. Marigo, Revisiting brittle fracture as an energy minimization problem, *J. Mech. Phys. Solids* 46 (8) (1998) 1319–1342.
- [28] A.A. Griffith, The phenomena of rupture and flow in solids, *Phil. Trans. Roy. Soc. Lond. A* 221 (1921) 163–198.
- [29] Y. Heider, *Saturated Porous Media Dynamics with Application to Earthquake Engineering*, Dissertation, Report No. II-25 of the Institute of Applied Mechanics (CE), University of Stuttgart, Germany, 2012.
- [30] Y. Heider, B. Markert, A phase-field modeling approach of hydraulic fracture in saturated porous media, *Mech. Res. Commun.* 80 (2017) 38–46.
- [31] Y. Heider, B. Markert, Modelling of hydraulic fracturing and fluid flow change in saturated porous domains, *Proc. Appl. Math. Mech.* 17 (2017) 95–98, <http://dx.doi.org/10.1002/pamm.201710028>.
- [32] G.R. Irwin, Analysis of stresses and strains near the end of a crack traversing a plate, *J. Appl. Mech.* 24 (1957) 361–364.
- [33] C. Kuhn, R. Müller, A continuum phase field model for fracture, *Eng. Fract. Mech.* 77 (18) (2010) 3625–3634.
- [34] S. Lee, A. Mikelic, M.F. Wheeler, T. Wick, Phase-field modeling of proppant-filled fractures in a poroelastic medium, *Comput. Methods Appl. Mech. Engrg.* 312 (2016) 509–541.
- [35] L. Li, C. Tang, G. Li, S. Wang, Z. Liang, Y. Zhang, Numerical simulation of 3d hydraulic fracturing based on an improved flow-stress-damage model and a parallel

- FEM technique, *Rock Mech. Rock Eng.* 45 (5) (2012) 801–818.
- [36] G. Liu, Q. Li, M.A. Msekhi, Z. Zuo, Abaqus implementation of monolithic and staggered schemes for quasi-static and dynamic fracture phase-field model, *Comput. Mater. Sci.* 121 (2016) 35–47.
- [37] B. Markert, A constitutive approach to 3-d nonlinear fluid flow through finite deformable porous continua, *Transp. Porous Med.* 70 (3) (2007) 427–450.
- [38] B. Markert, A survey of selected coupled multifield problems in computational mechanics, *J. Coupled Syst. Multiscale Dyn.* 27 (2013) 22–48.
- [39] B. Markert, Y. Heider, Coupled multi-field continuum methods for porous media fracture, in: M. Mehl, M. Bischoff, M. Schäfer (Eds.), *Recent Trends in Computational Engineering – CE2014, Lecture Notes in Computational Science and Engineering*, vol. 105, Springer International Publishing, 2015, pp. 167–180.
- [40] B. Markert, Y. Heider, W. Ehlers, Comparison of monolithic and splitting solution schemes for dynamic porous media problem, *Int. J. Numer. Meth. Eng.* 82 (2010) 1341–1383.
- [41] C. Miehe, F. Aldakheel, S. Teichtmeister, Phase-field modeling of ductile fracture at finite strains: a robust variational-based numerical implementation of a gradient-extended theory by micromorphic regularization, *Int. J. Numer. Meth. Eng.* 111 (9) (2017) 816–863.
- [42] C. Miehe, M. Hofacker, L.-M. Schänzel, F. Aldakheel, Phase field modeling of fracture in multi-physics problems. Part II. Coupled brittle-to-ductile failure criteria and crack propagation in thermo-elastic–plastic solids, *Comput. Methods Appl. Mech. Engrg.* 294 (2015) 486–522.
- [43] C. Miehe, M. Hofacker, F. Welschinger, A phase field model for rate-independent crack propagation: robust algorithmic implementation based on operator splits, *Comput. Methods Appl. Mech. Engrg.* 199 (45) (2010) 2765–2778.
- [44] C. Miehe, D. Kienle, F. Aldakheel, S. Teichtmeister, Phase field modeling of fracture in porous plasticity: a variational gradient-extended Eulerian framework for the macroscopic analysis of ductile failure, *Comput. Methods Appl. Mech. Engrg.* 312 (Supplement C) (2016) 3–50.
- [45] C. Miehe, S. Mauthe, Phase field modeling of fracture in multi-physics problems. Part III. Crack driving forces in hydro-poro-elasticity and hydraulic fracturing of fluid-saturated porous media, *Comput. Methods Appl. Mech. Engrg.* 304 (2016) 619–655.
- [46] C. Miehe, L.-M. Schänzel, H. Ulmer, Phase field modeling of fracture in multi-physics problems. Part I. Balance of crack surface and failure criteria for brittle crack propagation in thermo-elastic solids, *Comput. Methods Appl. Mech. Engrg.* 294 (2015) 449–485.
- [47] C. Miehe, F. Welschinger, M. Hofacker, Thermodynamically consistent phase-field models of fracture: variational principles and multi-field fe implementations, *Int. J. Numer. Meth. Eng.* 83 (10) (2010) 1273–1311.
- [48] A. Mikelić, M.F. Wheeler, T. Wick, A phase-field method for propagating fluid-filled fractures coupled to a surrounding porous medium, *Multiscale Model Simul.* 13 (1) (2015) 367–398.
- [49] A. Mikelić, M.F. Wheeler, T. Wick, A quasi-static phase-field approach to pressurized fractures, *Nonlinearity* 28 (5) (2015) 1371–1399.
- [50] N. Moës, T. Belytschko, Extended finite element method for cohesive crack growth, *Eng. Fract. Mech.* 69 (7) (2002) 813–833.
- [51] M.A. Msekhi, J.M. Sargado, M. Jamshidian, P.M. Areias, T. Rabczuk, Abaqus implementation of phase-field model for brittle fracture, *Comput. Mater. Sci.* 96 (2015) 472–484.
- [52] S.P. Patil, Y. Heider, C. Hernandez-Padilla, E. Cruz-Chú, B. Markert, A comparative molecular dynamics-phase-field modeling approach to brittle fracture, *Comput. Methods Appl. Mech. Engrg.* 312 (8) (2016) 117–129.
- [53] G. Pijaudier-Cabot, F. Dufour, M. Choinska, Permeability due to the increase of damage in concrete: from diffuse to localized damage distributions, *J. Eng. Mech.-ASCE* 135 (9) (2009) 1022–1028.
- [54] A. Prohl, *Projection and Quasi-compressibility Methods for Solving the Incompressible Navier-Stokes Equations*, Springer, 1997.
- [55] B.A. Schrefler, S. Secchi, L. Simoni, On adaptive refinement techniques in multi-field problems including cohesive fracture, *Comput. Methods Appl. Mech. Engrg.* 195 (4) (2006) 444–461.
- [56] S. Secchi, B. Schrefler, A method for 3-d hydraulic fracturing simulation, *Int. J. Numer. Anal. Met.* 178 (1–2) (2012) 245–258.
- [57] S. Secchi, B.A. Schrefler, Hydraulic fracturing and its peculiarities, *Asia Pac. J. Comput. Eng.* 1 (1) (2014) 1–21.
- [58] C. Truesdell, *Thermodynamics of diffusion*, in: C. Truesdell (Ed.), *Rational Thermodynamics*, second ed., Springer-Verlag, New York, 1984, pp. 219–236.
- [59] K. Weinberg, C. Hesch, A high-order finite deformation phase-field approach to fracture, *Continuum Mech. Thermodyn.* (2015), <http://dx.doi.org/10.1007/s00161-015-0440-7>.